Frequency-encoded two-photon excited fluorescence microscopy

Sandro Heuke, Carla Silva Martins, Rémi André, Loïc Le Goff, Hervé Rigneault

Frequency-encoded two-photon excited fluorescence microscopy (FE-2PEF)

SANDRO HEUKE[1,*], CARLA SILVA MARTINS[1], RÉMI ANDRÉ[1], LOIC LEGOFF[1], AND HERVÉ RIGNEAULT[1,*]

[1] Aix Marseille Univ, CNRS, Centrale Marseille, Institut Fresnel, Marseille, France.
[*] Corresponding authors: sandro.heuke@fresnel.fr & herve.rigneault@fresnel.fr

Compiled March 14, 2024

Two-photon excited fluorescence (2PEF) microscopy is the most popular nonlinear imaging method of biomedical samples. State-of-the art 2PEF microscopes use multiple detectors and spectral filter sets to discriminate different fluorophores based on their distinct emission behavior (emission discrimination). One drawback of 2PEF is that fluorescence photons outside the filter transmission range are inherently lost, thereby reducing the imaging efficiency and speed. Furthermore, emission discrimination of different fluorophores may fail if their emission profiles are too similar. Here, we present an alternative 2PEF method that discriminates fluorophores based on their excitation spectra (excitation discrimination). For excitation we use two lasers of different wavelengths (ω_1, ω_2) resulting in excitation energies at $2\omega_1$, $2\omega_2$ and the mixing energy ω_1+ω_2. Both lasers are frequency-encoded (FE) by an intensity modulation at distinct frequencies while all 2PEF emission is collected on a single detector. The signal is fed into a lockin-amplifier and demodulated at various frequencies simultaneously. A customized non-negative matrix factorization (NNMF) then generates fluorescence images that are free of cross-talk. Combining FE-2PEF with multiple detectors has the potential to enable the simultaneous imaging of an unprecedented number of fluorophores.

http://dx.doi.org/10.1364/ao.XX.XXXXXX

Two-photon excited fluorescence (2PEF) is the most popular contrast mechanism in non-linear microscopy [1, 2]. It combines high sensitivity with the ability for 3D sectioning, low photo-toxicity and moderate experimental costs [3]. As a major challenge in 2PEF microscopy, multiple fluorophores must be distinguished in space and time simultaneously. To parallelize the image acquisition of multiple fluorophores, Mahou et al. applied synchronized excitation pulses at two different wavelengths simultaneously and collected the fluorescence emission by multiple detectors with distinct optical filter sets (emission discrimination) [4]. This dual-color excitation configuration was recently extended to a wider range of fluorophores [5] and samples [6], light-sheet excitation [7] and 3-photon microscopy [8]. The distinction of fluorophores based on their emission profiles feature the advantage that commercially available laser scanning microscopes with multiple detectors are readily transformed to multi-color 2PEF microscopes by simply exchanging the excitation laser source but also features various disadvantages: (1) fluorescence photons offside the filter transmission window are lost compromising the imaging speed or signal to noise ratio. (2) The artifact-free separation of fluorophore requires weakly overlapping emission spectra which is not always the case. (3) Multiple detectors and filter sets are expensive and potentially waste space.

To overcome these limitations, we present a 2PEF microscopy scheme that isolates the fluorophore contribution by their excitation profile [9, 10]. Our experimental set-up is presented in Fig. 1a. A detailed description is also provided in supplementary information. Two lasers of color ω_1 and ω_2 are generated with a pump laser source and optical parametric oscillator. They are jointly focused onto the sample, exciting two-photon fluorophores at $2\omega_1$, $2\omega_2$ as well as at the photon-mixing energy $\omega_1 + \omega_2$ [4]. Laser 1 (ω_1) and Laser 2 (ω_2) are intensity modulated at the frequencies f_1 and f_2, respectively. A single detector collects all the fluorescence emission from all the fluorophores. The signal arising from the detector is demodulated simultaneously by a lockin amplifier at the zero frequency (direct current, DC) as well as at the frequencies f_1, f_2 and f_1-f_2. To remove fluorophore cross-talk, we apply a non-negative matrix factorization (NNMF) retrieving images of the true fluorophore distribution [9]. An advantage of our frequency-encoded approach is that a single detector is required, while the emission filter set is replaced by a simple short-pass filter blocking the excitation wavelength. Thus, all the fluorescent emission is collected, minimizing the losses due to overlapping emission spectra.

The remainder of this paper is organized as follows: First, we derive an expression that outlines which fluorophore contributes to which frequency channel. Second, we demonstrate FE-2PEF's imaging of stained U2OS osteosarcoma cells and show the merits of NNMF as a fluorescence unmixing procedure. Finally, we discuss situations where FE-2PEF has advantages over conventional 2PEF imaging with several detectors.

For an intuitive understanding of FE-2PEF, we derive an expression that determines which modulation frequency of laser excitation contributes, via fluorescence radiation, to which detection channel. For this purpose, we assume that exactly 3 fluorophores (a,b,c) are present within the sample and that each

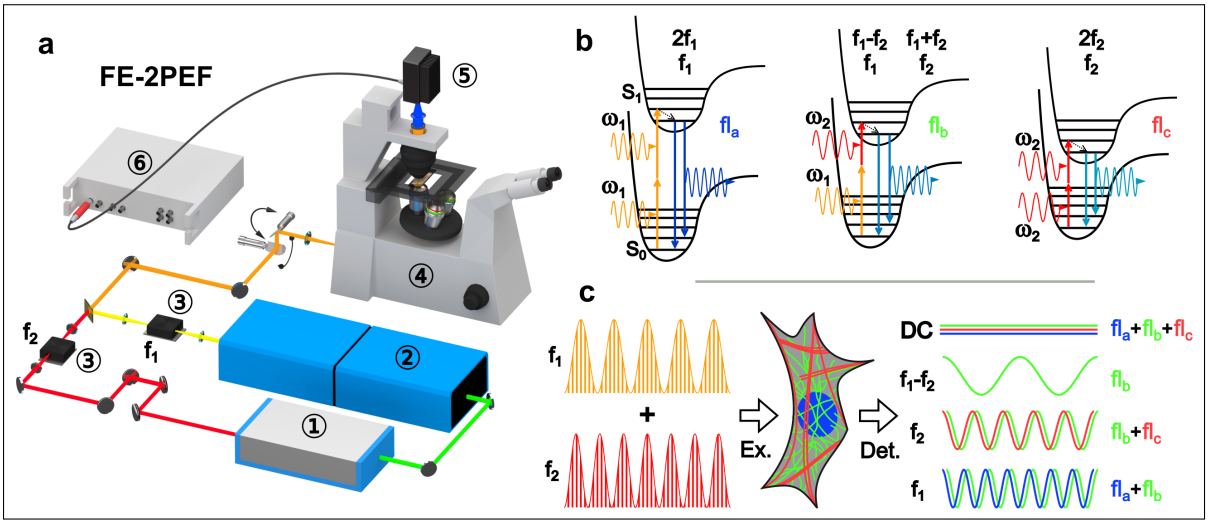

Fig. 1. FE-2PEF principle and experimental setup: a) 1 pump laser source, 2 optical parametric oscillator (OPO), 3 acousto-optical modulators (AOM), 4 laser scanning microscope, 5 photo-multiplier tube (PMT), 6 Lockin amplifier b) Energy diagrams of 3 different fluorophores that are responsive to an excitation at $2\omega_1$, ω_1+ω_2 and $2\omega_2$ (left to right). c) The laser at ω_1 and ω_2 are modulated at f_1 and f_2, respectively. Fluorescence radiation is detected at DC, f_1, f_2 and f_1-f_2. Only the difference frequency channel f_1-f_2 is pure, i.e. contains signal of only one fluorophore.

of these fluorophores is uniquely excited by $2\omega_1(fl_a)$, $2\omega_2(fl_b)$ or $\omega_1+\omega_2(fl_c)$ excluding any spectral cross-talk (Fig. 1b). In a second step, we shall investigate the more realistic case where spectral cross-talk cannot be excluded and derive methods for the separation of each fluorophore's local distribution and contribution to the individual channel.

For the sake of simplicity, we assume a perfect sinusoidal modulation of both modulated laser beams at f_1 and f_2, respectively. Excluding saturation effects, the measured fluorescence intensity follows the square of the excitation intensity:

$$I_{Ex} = [I_1(1+\cos f_1) + I_2(1+\cos f_2)]^2 \quad (1)$$

$$= \left(\frac{3}{2}I_1^2 + \frac{3}{2}I_2^2 + 2I_1I_2\right)\cos f_{DC} + 2(I_1^2 + I_1I_2)\cos f_1 \quad (2)$$
$$+ 2(I_2^2 + I_1I_2)\cos f_2 + \frac{1}{2}I_1^2\cos(2f_1) + \frac{1}{2}I_2^2\cos(2f_2)$$
$$+ I_1I_2\cos(f_1 - f_2) + I_1I_2\cos(f_1 + f_2)$$

Where I_1=$I_1(\omega_1)$ and I_2=$I_2(\omega_2)$. To arrive at Eq. 2, we used the identities $\cos^2 f = (1+\cos 2f)/2$ and $2\cos f_1 \cos f_2 = \cos(f_1 - f_2) + \cos(f_1 + f_2)$. Further, we assumed that f_1>f_2 and $f_{DC} = 0Hz$ is the direct current modulation frequency. Evidently, the fluorophores a, b and c follow the dynamics of the excitation intensity terms I_1^2, I_2^2 and I_1I_2, respectively. Interpreting Eq. 2, the DC channel at zero modulation frequency contains contributions of all 3 fluorophores. The output of the DC channel of the locklin amplifier, therefore, resembles the image that a single PMT would capture using an unmodulated dual-color 2PEF excitation approach. On the contrary, the FE-2PEF image extracted at f_1+f_2 or, equivalently, f_1-f_2 provides exclusively information about fluorophores c, while the FE-2PEF images at $2f_1$ and $2f_2$ map the distribution of the fluorophores a and b, respectively. Finally, we observe a modulation cross-talk of fluorophore c with fluorophores a and b, affecting the FE-2PEF images at f_1 and f_2, respectively. Thus, the FE-2PEF approach results up to 6 different image channels (at DC, f_1, f_2, $2f_1$, $2f_2$, f_1-f_2) with varying contributions from the 3 different fluorophores.

Since we have assumed fluorophores with no spectral cross-talk, the FE-2PEF channels at $2f_1$, $2f_2$ and f_1-f_2 would each uniquely highlight one fluorophore. However, we have found experimentally that the $2f_1$ and $2f_2$ images are overwhelmed by noise. Though Eq. 2 predicts a comparably weak signal level for the second harmonic channels ($2f_1$ and $2f_2$) we do not have a conclusive explanation for this observation. The low image quality might be a result of the non-linearity of our detector or an excitation saturation effect of the fluorophores. Algorithms for fluorphore unmixing work best with low noise images and become more robust with the addition of more image data points. We unmixed, therefore, the FE-2PEF channels using the frequencies DC, f_1, f_2 and f_1-f_2, but did not take $2f_1$ and $2f_2$ into account. As described above, the DC, f_1 and f_2 channel feature a modulation cross-talk meaning that several fluorophores contribute to the same channel - see also Fig.1c. For all practical concerns, this modulation cross-talk can be treated as additional spectral cross-talk. For this reason, we now drop the distinction of modulation and spectral cross-talk and consider only the sum of both phenomena (and refer to it just as cross-talk). Restricting our attention to the four FE-2PEF channels DC, f_1, f_2 and f_1-f_2 and considering 3 fluorophores with non-negligible cross-talk, the problem under investigation can be phrased as - What is the relative contribution of each fluorophore within each channel? To answer this question, let us first consider the following mixing model:

$$\begin{pmatrix} S_{DC} \\ S_{f_1} \\ S_{f_2} \\ S_{(f_1-f_2)} \end{pmatrix} = \begin{pmatrix} \sigma_{a;DC} & \sigma_{b;DC} & \sigma_{c;DC} \\ \sigma_{a;f_1} & \sigma_{b;f_1} & \sigma_{c;f_1} \\ \sigma_{a;f_2} & \sigma_{b;f_2} & \sigma_{c;f_2} \\ \sigma_{a;f_1-f_2} & \sigma_{b;f_1-f_2} & \sigma_{c;f_1-f_2} \end{pmatrix} \begin{pmatrix} c_a \\ c_b \\ c_c \end{pmatrix} \quad (3)$$

or

$$\mathbf{S} = \mathbf{\Sigma C} \quad (4)$$

where $\mathbf{S}$ is the FE-2PEF signal vector that represents the four channels, $\mathbf{\Sigma}$ contains the individual FE-2PEF signatures of each fluorophore and $\mathbf{C}$ contains the fluorophore concentration for each image pixel.

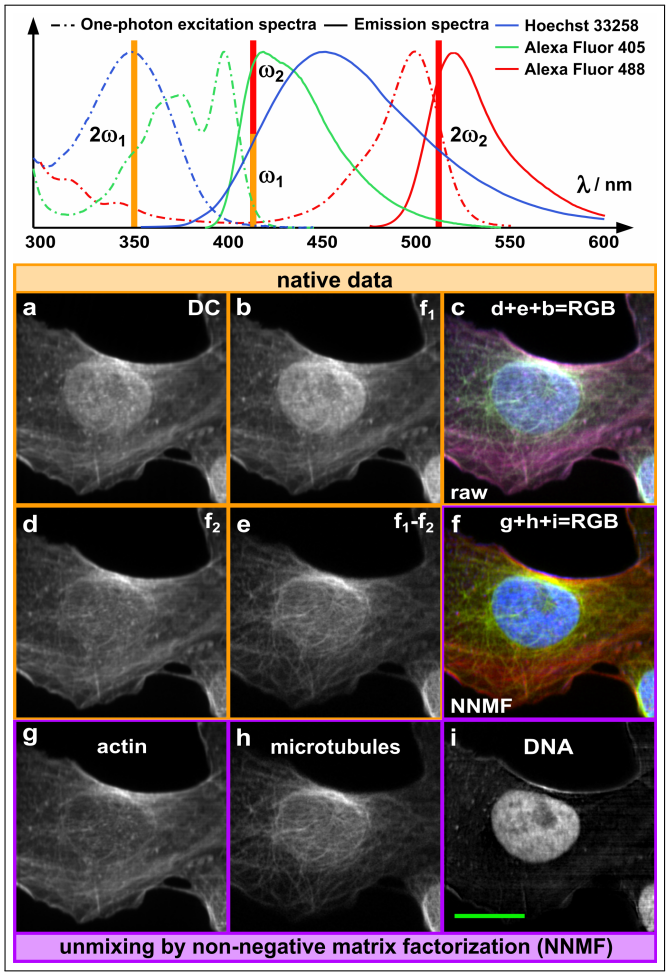

Fig. 2. FE-2PEF imaging of U2OS osteosarcoma cells which were stained by Hoechst 33258 (nucleus), Alexa Fluor 488 (actin) and Alexa Fluor 405 (microtubules). Subfigures a,b,d and e display the FE-2PEF raw images for the demodulation frequencies DC(= 0 Hz), f_1, f_2 and f_1-f_2. Subfigures g, h and i show the result after non-negative matrix factorization (NNMF). The SubFig. c and f outline the composite RGB images arising from raw data (d+e+b) or after NNMF signal unmixing (g+h+i). Pixel dwell time: 40 µs. Total image acquisition time: 40 s. The green scale bar equals 20 µm. Top: emission and one-photon excitation spectra (1PEF) are shown [11].

When $\mathbf{\Sigma}$ is known from previous experiments, the inversion of Eq. 4 is readily achieved for every single image point by, e.g. least square fitting via the computation of the pseudo-inverse $\mathbf{\Sigma}^{\dagger}$ such as $\mathbf{C} = \mathbf{\Sigma}^{\dagger}\mathbf{S}$.
For any lab routine, $\mathbf{\Sigma}$ would have to be characterized just before the actual experiment starts, since a power drop of one of the excitation lasers or any mismatch of the superposition of the excitation foci modifies $\mathbf{\Sigma}$. Thus, it is preferable to use methods that allow retrieving the coefficient matrix $\mathbf{\Sigma}$ and the fluorophore's contributions $\mathbf{C}$ simultaneously [9, 12]. For FE-2PEF, neither the coefficient matrix nor the fluorophore concentration matrix contain negative values. Hence, $\mathbf{\Sigma}$ and $\mathbf{S}$ can be estimated by using a Non-Negative Matrix Factorization (NNMF) algorithm [13]. To stabilize the matrix estimation, it is common practice to regularize the inversion problem by introducing prior information. Since 2PEF images of stained cells often feature dark areas, we impose to the fluorophore concentration matrix to be sparse by using a L1-norm penalisation. To avoid ill-conditioned problems, we applied in addition a L2-norm penalization.
Accounting for these considerations, we selected for fluorophore unmixing the basic NNMF algorithm that is implemented in Matlab [14, 15] and added L1- and L2-norm penalizations. Our NNMF algorithm aims to minimize the following expression:

$$||\mathbf{S} - \mathbf{\Sigma C}||_F^2 + \alpha_1 ||\mathbf{C}||_1 + \alpha_2 ||\mathbf{C}||_F^2 \text{ subject to } \mathbf{\Sigma} \geq 0, \mathbf{C} \geq 0 \quad (5)$$

where the penalization parameters α_1 and α_2 are set to 0.1 for the unmixing results presented in Fig. 2. The NNMF algorithm starts from a random guess of $\mathbf{\Sigma}$ and $\mathbf{C}$ and improves the factorization, at each iteration n, following the update formula:

$$\mathbf{\Sigma}_{n+1} = \mathbf{\Sigma}_n \odot \frac{\mathbf{S}\mathbf{C}_n^T}{\mathbf{\Sigma}_n \mathbf{C}_n \mathbf{C}_n^T} \quad (6)$$

and

$$\mathbf{C}_{n+1} = \mathbf{C}_n \odot \frac{\mathbf{\Sigma}_{n+1}^T \mathbf{S}}{\mathbf{\Sigma}_{n+1}^T \mathbf{\Sigma}_{n+1} \mathbf{C}_n + \alpha_1 + \alpha_2 \mathbf{C}_n} \quad (7)$$

where $\odot$ is the element-wise product.

Further details about the derivation of the Eqs. 6 and 7 can be found within the supplementary information.
For demonstration of FE-2PEF imaging, we selected a U2OS osteosarcoma cell line that was labeled with Hoechst 33258, Alexa Fluor 405 and Alexa Fluor 488 outlining the distribution or location of the nucleus (through DNA labeling), microtubules and actin filaments, respectively - see Fig. 2. A description of the sample preparation can be found within the supplementary information. Actin is a globular protein forming microfilaments in eukaryotic cells as part of the cytoskeleton. It contributes to cell mobility, contraction, or migration [16]. Microtubules also assemble into filaments as part of the cytoskeleton. They provide tracks for motor-driven intracellular transport and provide cues for the spatial organization of cells [17]. The nucleus contains the major part of the cells DNA and, therefore, can be considered as the cell's library and control center [18]. Thus, monitoring the location and number of the nuclei as well as the structure and abundance of actin and microtubules provide solid indicators about the cells health, metabolic activity and motility.
Here, we selected the dyes Hoechst 33258 and Alexa Fluor 405 and 488 for their distinct two-photon absorption behavior at the excitation wavelength applied (697 nm, 1030 nm) [19, 20]. From the top of Fig. 2, it is evident that the fluorescence emission spectra of the Hoechst dye vastly overlaps with the those of the Alexa Fluor dyes rendering the selection of suitable spectral filter set a challenging task for any 2PEF experiment using multiple detectors. This issue is less pronounced for our FE-2PEF approach because the fluorophore distinction is based on the excitation profile which is better separated than the emission curves. To obtain the results presented in Fig. 2, the stained U2O2 cells were imaged using the excitation wavelength 697 nm (ω_1) and 1030 nm (ω_2) leading to one-photon equivalent excitations at 349 nm, 416 nm and 515 nm. Both laser were intensity modulated at the frequencies 4.6 MHz (f_1,ω_1) and 3.1 MHz (f_2,ω_2).

The lockin amplifier demodulated the fluorescence signal at 0 Hz (DC), 1.5 MHz (f_1-f_2), 3.1 MHz (f_2) and 4.6 MHz (f_1), simultaneously. Raw FE-2PEF image data are displayed in Fig. 2 a, b, d and e and superimposed in Fig. 2 c. As expected, we observe dominant contributions of the nucleus, actin and microtubules in the Fig. 2 b, d, e, respectively. The RGB composite of these raw images (Fig. 2 c) reveals the green web of microtubules, the denser network of actin microfilaments in red and the nucleus in blue. However, as expected, these raw images suffer from a non negligeable crosstalk. this is most notable in the f_1 image (Fig. 2 b), as no Hoechst staining should be observed outside the nucleus. To remove the cross-talk, we applied the NNMF unmixing introduced above. The result of the NNMF are displayed in Figs. 2 g, h and i, which display respectively actin, microtubules and DNA, as well as in the RGB composite image Fig. 2 f. Crosstalk between the channels has visibly been considerably reduced. For example, signal corresponding to staining of DNA (Fig. 2 i) is now strictly confined to the nucleus. The NNMF composite image (Fig. 2 f) outlines each cellular component with an improved contrast with respect to the composite image of raw FE-2PEF images (Fig. 2 c). Furthermore, the image brightness of individual NNMF channels scales linear to the fluorophore concentration.

Having established the theory and experimental feasibility of FE-2PEF, we now discuss when to use it. FE-2PEF features several advantages. First, it captures all the fluorescence light, increasing the overall signal level, which is of high value to overcome additive noise sources such as detector dark noise or ambient light. Second, the excitation-based fluorophore separation used in FE-2PEF yields better discrimination when the fluorophores emission spectra overlap substantially. Third, the detection is more compact and the signal collection efficiency is equal for all colors. Fourth, FE-2PEF can rapidly adapt to a wide range of fluorophore characteristics by simply changing the excitation wavelength of the tunable laser source. Thus, FE-2PEF is readily adapted to new fluorophores with potentially unknown spectral characteristics.

Nevertheless, FE-2PEF also features some disadvantages: (1) The modulation related fluorophore cross-talk requires the application of unmixing algorithm such as the NNMF to retrieve images that contain information about only one species (except for the f_1-f_2 channel). (2) The detector gain is the same for all fluorophores, though the fluorescence brightness may vary substantially. Balancing of the signal strength must be achieved by adjusting the laser power, pulse overlap or the fluorophore concentration. (3) The fluorescence signal of any fluorophore increases the shot-noise level for every channel and the dynamic range of the detector is shared over all contributing emitters.

In summary, if FE-2PEF performs better or worse than multi-detector 2PEF depends on the individual experimental conditions. FE-2PEF is the method of choice if additive noise is the dominant noise source. Furthermore, FE-2PEF will perform well if the fluorophores are spatially well separated within the sample (sparsity constrain) to avoid noise cross-talk. In multi-modal approaches combining, e.g., coherent anti-Stokes Raman scattering (CARS), second harmonic generation (SHG) and multi-color 2PEF, FE-2PEF's compact single-element detection scheme may reduce the detection system to a manageable size and complexity. However, multi-detector 2PEF implementation has an edge over FE-2PEF for the important application scenario of overlapping fluorophore distributions featuring large signal level differences due to the possibility to adjust the gain independently for each channel as well as the reduced signal and noise cross-talk. Still, FE-2PEF and multi-detector 2PEF do not exclude each other but are complementary. Extending FE-2PEF to multiple detectors will yield a better fluorophore discrimination than any of the 2 concepts alone. Thus, a multi-detector FE-2PEF microscope holds the potential to image and separate more fluorophores simultaneously than it was ever possible before.

FUNDING INFORMATION

We acknowledge financial support from the Centre National de la Recherche Scientifique (CNRS), ANR grants (ANR-11-IDEX-0001-02, ANR-10-INSB-04-01, ANR-11-INSB-0006, ANR-16-CONV-0001, ANR-21-ESRS-0002 IDEC), INSERM (PC201508, 18CP128-00, 22CP139-00). This project has received funding from European Union's Horizon 2020 EU ICT 101016923 CRIMSON and European Research Council (ERC), SpeckleCARS 101052911.

DISCLOSURE

The authors declare no conflict of interest.

SUPPORTING INFORMATION

See Supplement 1 for supporting content.

REFERENCES

1. W. Denk, J. Strickler, and W. Webb, Science **248**, 73 (1990).
2. J. R. Lakowicz, *Principles of Fluorescence Spectroscopy* (Springer-Verlag GmbH, 2007).
3. P. T. C. So, C. Y. Dong, B. R. Masters, and K. M. Berland, Annu. Rev. Biomed. Eng. **2**, 399 (2000).
4. P. Mahou, M. Zimmerley, K. Loulier, K. S. Matho, G. Labroille, X. Morin, W. Supatto, J. Livet, D. Débarre, and E. Beaurepaire, Nat. Methods **9**, 815 (2012).
5. A. Rakhymzhan, R. Leben, H. Zimmermann, R. Günther, P. Mex, D. Reismann, C. Ulbricht, A. Acs, A. U. Brandt, R. L. Lindquist, T. H. Winkler, A. E. Hauser, and R. A. Niesner, Sci. Reports **7** (2017).
6. C. Stringari, L. Abdeladim, G. Malkinson, P. Mahou, X. Solinas, I. Lamarre, S. Brizion, J.-B. Galey, W. Supatto, R. Legouis, A.-M. Pena, and E. Beaurepaire, Sci. Reports **7** (2017).
7. P. Mahou, J. Vermot, E. Beaurepaire, and W. Supatto, Nat. Methods **11**, 600 (2014).
8. K. Guesmi, L. Abdeladim, S. Tozer, P. Mahou, T. Kumamoto, K. Jurkus, P. Rigaud, K. Loulier, N. Dray, P. Georges, M. Hanna, J. Livet, W. Supatto, E. Beaurepaire, and F. Druon, Light. Sci. & Appl. **7** (2018).
9. E. T. Garbacik, M. Sanz-Paz, K. J. Borgman, F. Campelo, and M. F. Garcia-Parajo, Biophys. J. **115**, 725 (2018).
10. M. Tovar, S. Hengoju, T. Weber, L. Mahler, M. Choudhary, T. Becker, and M. Roth, Anal. Chem. **91**, 3055 (2019).
11. T. J. Lambert, Nat. Methods **16**, 277 (2019).
12. A.-S. Montcuquet, L. Hervé, F. P. N. Y. Garcia, J.-M. Dinten, and J. I. Mars, J. Biomed. Opt. **15**, 056009 (2010).
13. D. Lee and H. S. Seung, "Algorithms for non-negative matrix factorization," in *Advances in Neural Information Processing Systems,* , vol. 13 T. Leen, T. Dietterich, and V. Tresp, eds. (MIT Press, 2000).
14. M. W. Berry, M. Browne, A. N. Langville, V. P. Pauca, and R. J. Plemmons, Comput. Stat. & Data Analysis **52**, 155 (2007).
15. MATLAB, *Version 9.8.0.1323502 (R2020a)* (The MathWorks Inc., Natick, Massachusetts, 2020).
16. R. Dominguez and K. C. Holmes, Annu. Rev. Biophys. **40**, 169 (2011).
17. H. V. Goodson and E. M. Jonasson, Cold Spring Harb. perspectives biology **10**, a022608 (2018).
18. T. Guo and Y. Fang, Front. Plant Sci. **5** (2014).
19. J. Trägardh, G. Robb, R. Amor, W. Amos, J. Dempster, and G. McConnell, J. Microsc. **259**, 210 (2015).
20. V. L. Anderson and W. W. Webb, BMC Biotechnol. **11** (2011).

REFERENCES

1. W. Denk, J. Strickler, and W. Webb, Science **248**, 73 (1990).
2. J. R. Lakowicz, *Principles of Fluorescence Spectroscopy* (Springer-Verlag GmbH, 2007).
3. P. T. C. So, C. Y. Dong, B. R. Masters, and K. M. Berland, Annu. Rev. Biomed. Eng. **2**, 399 (2000).
4. P. Mahou, M. Zimmerley, K. Loulier, K. S. Matho, G. Labroille, X. Morin, W. Supatto, J. Livet, D. Débarre, and E. Beaurepaire, Nat. Methods **9**, 815 (2012).
5. A. Rakhymzhan, R. Leben, H. Zimmermann, R. Günther, P. Mex, D. Reismann, C. Ulbricht, A. Acs, A. U. Brandt, R. L. Lindquist, T. H. Winkler, A. E. Hauser, and R. A. Niesner, Sci. Reports **7** (2017).
6. C. Stringari, L. Abdeladim, G. Malkinson, P. Mahou, X. Solinas, I. Lamarre, S. Brizion, J.-B. Galey, W. Supatto, R. Legouis, A.-M. Pena, and E. Beaurepaire, Sci. Reports **7** (2017).
7. P. Mahou, J. Vermot, E. Beaurepaire, and W. Supatto, Nat. Methods **11**, 600 (2014).
8. K. Guesmi, L. Abdeladim, S. Tozer, P. Mahou, T. Kumamoto, K. Jurkus, P. Rigaud, K. Loulier, N. Dray, P. Georges, M. Hanna, J. Livet, W. Supatto, E. Beaurepaire, and F. Druon, Light. Sci. & Appl. **7** (2018).
9. E. T. Garbacik, M. Sanz-Paz, K. J. Borgman, F. Campelo, and M. F. Garcia-Parajo, Biophys. J. **115**, 725 (2018).
10. M. Tovar, S. Hengoju, T. Weber, L. Mahler, M. Choudhary, T. Becker, and M. Roth, Anal. Chem. **91**, 3055 (2019).
11. T. J. Lambert, Nat. Methods **16**, 277 (2019).
12. A.-S. Montcuquet, L. Hervé, F. P. N. Y. Garcia, J.-M. Dinten, and J. I. Mars, J. Biomed. Opt. **15**, 056009 (2010).
13. D. Lee and H. S. Seung, "Algorithms for non-negative matrix factorization," in *Advances in Neural Information Processing Systems,* , vol. 13 T. Leen, T. Dietterich, and V. Tresp, eds. (MIT Press, 2000).
14. M. W. Berry, M. Browne, A. N. Langville, V. P. Pauca, and R. J. Plemmons, Comput. Stat. & Data Analysis **52**, 155 (2007).
15. MATLAB, *Version 9.8.0.1323502 (R2020a)* (The MathWorks Inc., Natick, Massachusetts, 2020).
16. R. Dominguez and K. C. Holmes, Annu. Rev. Biophys. **40**, 169 (2011).
17. H. V. Goodson and E. M. Jonasson, Cold Spring Harb. perspectives biology **10**, a022608 (2018).
18. T. Guo and Y. Fang, Front. Plant Sci. **5** (2014).
19. J. Trägardh, G. Robb, R. Amor, W. Amos, J. Dempster, and G. McConnell, J. Microsc. **259**, 210 (2015).
20. V. L. Anderson and W. W. Webb, BMC Biotechnol. **11** (2011).